Wideband Active Region Metasurface Antennas

Marco Faenzi, D. Gonzalez-Ovejero, Stefano Maci

To cite this version:

Marco Faenzi, D. Gonzalez-Ovejero, Stefano Maci. Wideband Active Region Metasurface Antennas. IEEE Transactions on Antennas and Propagation, 2020, 68 (3), pp.1261-1272. 10.1109/TAP.2019.2940365 . hal-02338199

Wideband Active Region Metasurface Antennas

Marco Faenzi, David González-Ovejero, *Senior Member*, *IEEE*, and Stefano Maci, *Fellow*, *IEEE*

***Abstract*—Modulated metasurface (MTS) antennas with broadside beam rely on the interaction between a radially modulated equivalent impedance and a surface wave (SW) with cylindrical wave-front, launched by a point source. At the frequency where the SW wavelength matches the period of the impedance modulation, the -1 indexed (leaky) mode of the Floquet-mode expansion in cylindrical-coordinates provides a broadside beam. The mismatch between the SW wavelength and the period of the modulation imposes a limitation on the product bandwidth-gain. Here, we overcome this limitation by exponentially stretching the radial period of the impedance modulation. Doing so, an annular active region is generated on the antenna aperture, which moves from the antenna center to the circular rim as the frequency decreases. This mechanism enables a broadside beam over an extreme large bandwidth. We therefore extend significantly the applicability of these antennas, e.g., to requirements of 30 ± 1.5 dB gain over 30% bandwidths. Here, an analytical formulation is proposed to treat the active region migration and edge outgoing by a Fresnel-type transition function. This function predicts in closed form the antenna bandwidth and average gain. A more accurate gain versus frequency response is also introduced by an integral formula that accounts for the frequency dependent amplitude distribution of the aperture fields. The theory is validated by full-wave simulations and by measurements of a prototype realized by sub-wavelength elliptical patches. The presented results show that these antennas can provide a performance difficult to reach by any other flat antennas based on printed technology.**

***Index Terms*—metasurface antenna, surface-wave broadband antenna, circular polarization, leaky waves, impedance boundary conditions.**

I. INTRODUCTION

METASURFACES are often defined as the two-dimensional equivalent of metamaterials, and allow one to achieve unusual reflection/transmission properties of space waves [1]-[5] and/or to modify the dispersion properties of surface/guided waves [6]-[11]. The latter phenomenon has been applied to design a new generation of ultra-flat antennas [12]-[20], named modulated MTS antennas. They have attracted a lot of interest due to their low-profile, light weight, and simple feeding scheme. Typically, they consist of a textured surface made of either sub-wavelength patches printed on a grounded substrate or conductive pins protruding out of a metallic ground [21]-[22]. The MTS constitutive elements are arranged in a regular grid, and serve to synthesize modulated reactance patterns that enable the control of both the amplitude and phase of the aperture fields. In general, a surface-wave (SW) is gradually transformed into a leaky-wave (LW), owing to the SW interaction with a periodically modulated reactance. The modulation is tailored so the “-1”-indexed mode in the Floquet expansion of this periodic problem is located in the visible region. The sub-wavelength dimensions of the constitutive elements lend these antennas unique characteristics in terms of lightness and flatness, which renders them very appealing for space applications [16]. Moreover, current design methods for modulated MTS antennas are very effective and allow us to meet demanding capabilities such as high efficiency [23], dual polarization [24]-[25], beam shaping [26]-[27], multiple beams [28]-[30] and dual-band operation [31]-[32]. In turn, the multilayered MTS in [33] helps to improve the scanning range of frequency-scanning antennas. The 3-dB bandwidth (BW) of the single-layer MTS in [33] goes from 8.35 to 13.6 GHz with a scan angle ranging between 5º−63º. Unlike the work in [33], we want to maintain a fixed broadside beam while extending the bandwidth. To this end, we propose the use of a non-uniform modulation period.

The main drawback of conventional MTS antennas is their limitation in terms of product bandwidth gain. In particular, circular apertures with period d of the MTS modulation independent of the radial coordinate provide broadside high gain at the frequency where d matches the wavelength of the exciting SW. One can estimate the bandwidth as in [34], where an optimal choice of the amplitude modulation index m is assumed for antennas with radius $a>3\lambda_0$ (with λ_0 being the free-space wavelength at the center frequency f_0). Then, the fractional bandwidth is given by $\Delta f/f_0=1.2(a/\lambda_0)(v_g/c)$, where c is the speed of light in free space, and v_g is the group velocity of the SW at f_0 when it propagates along a uniform average impedance. In addition, the aperture gain in absence of losses (directivity) is $G=(2\pi a/\lambda_0)^2(a/\lambda_0)/(a/\lambda_0+2)$, for an optimal m [34]. In the case of electrically large antennas, the latter expressions provide a fractional bandwidth gain product approximately equal to $47(a/\lambda_0)(v_g/c)$. Practical values of $\Delta f/f_0$ may vary between 3% and 9% when the antenna gain goes from 40 to 28.5 dBi (see Fig. 5 in [34]). The previous

---

This work was developed under the European Space Agency co-financed contract no. 4000113714/15/NL/MH/ats within the framework of the Networking Partnering Initiative programme. The work of M. Faenzi and D. González-Ovejero has been supported by Région Bretagne under the Stratégie d’Attractivité Durable (SAD) volet 2 programme, contract no. SAD17012, and by the European Union through the European Regional Development Fund, in part by the French Region of Brittany, Ministry of Higher Education and Research, Rennes Métropole and Conseil Départemental 35 through the CPER Project STIC & Ondes.

M. Faenzi and D. González-Ovejero are with Univ Rennes, CNRS, IETR (Institut d’Électronique et de Télécommunications de Rennes), UMR 6164, 35000 Rennes, France

S. Maci is with Department of Information Engineering and Mathematics, University of Siena, Italy (e-mail: macis@dii.unisi.it).

expressions are only valid for the case of uniform period *d*. In this paper, we will disregard this assumption to obtain expressions for the more general case of a non-uniform modulation period.

The main reason for the bandwidth limitation is the mismatch between the periodicity of the modulation and the dispersive variation with frequency of the SW wavelength. This variation is mostly due to the dispersion in the substrate, and provokes a gradual reduction of the antenna gain at broadside. Nonetheless, one can improve the bandwidth by modifying the period of the equivalent reactance patterns on the MTS aperture. In the approach proposed here, the periodicity of the modulation is exponentially varied within a proper range along the aperture radius. This way, it is possible to locally maintain the coherence between the SW wavelength and the modulation period, thus keeping the desired pointing direction over a broader frequency range. We will apply this method, without any loss of generality, to the design of MTS consisting of sub-wavelength patches printed on a grounded slab.

The presentation is structured as follows. Section II establishes the reactance model adopted in the analysis. Section III analyzes the antenna efficiency in the SW wavelength domain by using an active-region formalism. This analysis assumes that the -1 indexed Floquet wave has constant amplitude on the surface, which leads to simple design formulas. Despite the impossibility of realizing this condition in practice, the closed form formulas obtained for this ideal case are very useful to carry out an initial design. In Section IV, we eliminate the assumption of uniform power density, introducing a more accurate model. This model relies on the definition of an equivalent canonical problem that locally matches the amplitude and phase of the reactance. Section V presents a validation of these formulations by full-wave Method of Moments (MoM) simulations of the homogenized impedance plane. In the same section, the ideal impedance is synthesized by small elliptical patches, and the resulting design fabricated and tested to demonstrate the feasibility of the concept with a realistic example. Conclusions are drawn in section VI.

II. Reactance Model And SW Dispersion

The studied modulated MTS antennas consist of circular apertures of radius *a*. In the following, we will represent vectors by bold characters, unit vectors by bold characters with carets, and tensors by bold characters underlined with double-bars. An exp(j*ωt*) time dependence, where *ω* is the angular frequency, is assumed and suppressed. Furthermore, *k* and *ζ* will denote the free-space wavenumber and impedance, respectively. For convenience, we will employ a cylindrical coordinate system centered on the circular aperture. Using the radial distance *ρ* and azimuth *φ* one can define a generic point on the aperture as $\boldsymbol{\rho} = \rho\cos\varphi\,\hat{\mathbf{x}} + \rho\sin\varphi\,\hat{\mathbf{y}}$. This reference system has $(\hat{\boldsymbol{\rho}},\hat{\boldsymbol{\varphi}})$ unit vectors. Fig. 1 shows a MTS made of metallic patches printed on a grounded dielectric substrate with thickness *h* and relative permittivity ε_r. The MTS constitutive elements are arranged in a square lattice with period *p*. We assume that the MTS cladding is placed at the *z*=0 plane, i.e., at the air-dielectric interface. Although we will particularize our analysis to circularly polarized antennas with a broadside pencil beam, the obtained results can also be used for linearly polarized antennas.

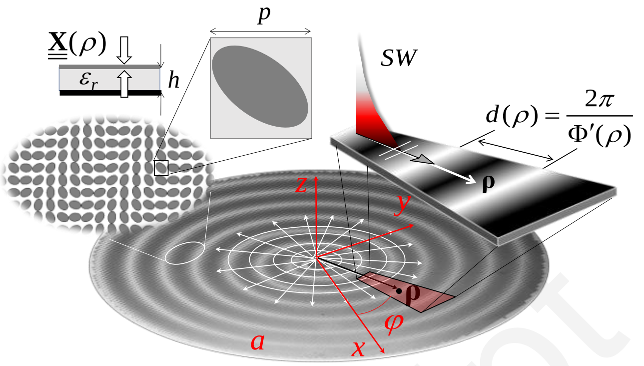

Fig. 1. Representation of the reference coordinate system and the transparent reactance pattern for the broadband MTS aperture. The source is a TM-SW launcher consisting of a vertical electric dipole placed at the geometrical center of the aperture.

A. Transparent Reactance Model

The MTS texture can be modeled by an equivalent reactance tensor $\underline{\underline{\mathbf{X}}}$, which relates the tangential electric and magnetic fields at the homogenized interface as [27]

$$\mathbf{E}_t = \mathrm{j}\underline{\underline{\mathbf{X}}}\cdot\hat{z}\times\left(\mathbf{H}_t\big|_{z=0^+} - \mathbf{H}_t\big|_{z=0^-}\right) \doteq \mathrm{j}\underline{\underline{\mathbf{X}}}\cdot\mathbf{J} \tag{1}$$

where $\hat{\mathbf{z}}$ is the normal to the MTS plane, $\mathbf{E}_t$ is the tangential electric field averaged at *z*=0, and $\mathbf{H}_t\big|_{z=0^+} - \mathbf{H}_t\big|_{z=0^-}$ represents the difference between the tangential magnetic fields on either side of the MTS. The discontinuity of $\mathbf{H}_t$ at the interface accounts for the current $\mathbf{J}$ flowing in the MTS.

We model the MTS cladding by an anisotropic "trans-parent" symmetric reactance tensor $\underline{\underline{\mathbf{X}}}$, which possesses an average $(1/A)\iint_A \underline{\underline{\mathbf{X}}}\,dA \approx \underline{\underline{\mathbf{I}}}\,\bar{X}_\rho$, where the integration is performed over the circular area *A*. In absence of losses, the symmetry of $\underline{\underline{\mathbf{X}}}$ ensures the realization feasibility of this ideal tensor. The components of $\underline{\underline{\mathbf{X}}}$ oscillate radially with the form

$$\begin{aligned}\underline{\underline{\mathbf{X}}} = \bar{X}_\rho \Big\{ \underline{\underline{\mathbf{I}}} + m(\rho)\Big[& \cos\left[\Phi(\rho)+\varphi\right]\left(\hat{\boldsymbol{\rho}}\hat{\boldsymbol{\rho}} - \hat{\boldsymbol{\varphi}}\hat{\boldsymbol{\varphi}}\right) \\ & -\sin\left[\Phi(\rho)+\varphi\right]\left(\hat{\boldsymbol{\rho}}\hat{\boldsymbol{\varphi}} + \hat{\boldsymbol{\varphi}}\hat{\boldsymbol{\rho}}\right)\Big]\Big\}\end{aligned} \tag{2}$$

where *m*(*ρ*) is a modulation index, *φ* is the azimuthal angle and Φ(*ρ*) is the phase of the modulation. From this phase, one can define the local period of the radial oscillation as $d(\rho) = 2\pi/\left(\Phi'(\rho)\right)$ (see the top right inset in Fig. 1). Similarly, given the function *d*(*ρ*) that defines the local period, one may retrieve Φ(*ρ*) through

$$\Phi(\rho) = \int_0^\rho \frac{2\pi}{d(\rho')}\,d\quad' + \Phi(0) \tag{3}$$

ρ

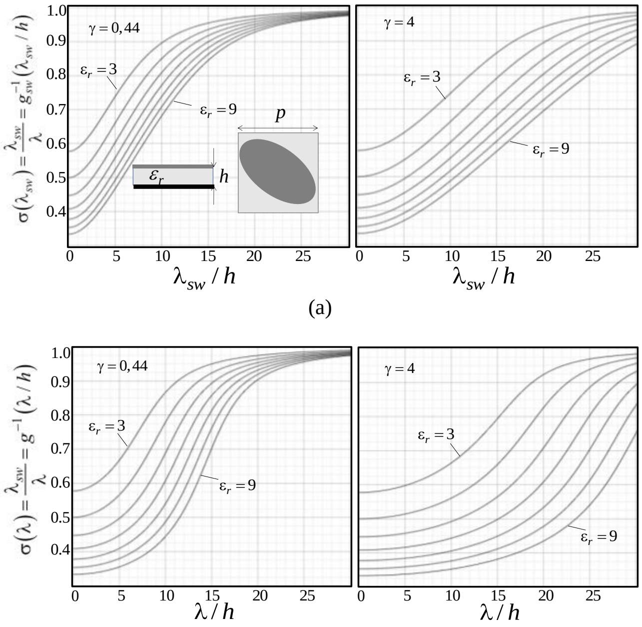

Fig. 2. Inverse functions of: (a) $g_{sw}(\lambda_{sw}/h)$ in (5), and (b) $g(\lambda/h)$ in (6) for various values of ε_r and for γ = 0.44 and γ = 4 in ranges of practical interest.

B. *SW dispersion and compression factor*

A proper implementation of (3) for broadband operation should take into account the variation of the SW wavelength with frequency. This variation is due to the dispersion of both the MTS and the grounded slab. In the homogenization regime, and provided that the MTS constitutive elements be non-resonant, we may write the average reactance value within a good approximation as $\bar{X}_\rho \approx -(\omega C)^{-1}$. In the range of frequency used in these antennas, the capacitance C depends on the geometry of the printed element (see the inset in Fig. 1) [35]. The reactance is modulated by changing the average capacitance C on the surface. To this end, one can gently change the dimensions of the printed elements. It is possible to prove [35]-[36] that, in a large frequency range, the capacitance C can be written as $C = \varepsilon_0 v_0 p(\varepsilon_r + 1)/2$, where v_0 is a geometric factor (typically between 0.5 and 1.5) and p is the side of the elementary square unit-cell (see the top-left inset in Fig. 1). Using $\bar{X}_\rho \approx -(\omega C)^{-1}$, the dispersion equation for the dominant TM SW can be written as

$$\frac{\lambda^2}{(2\pi)^2 h^2\left(\varepsilon_r - \lambda^2/\lambda_{sw}^2\right)} - \frac{\lambda}{2\pi\varepsilon_r h\sqrt{\lambda^2/\lambda_{sw}^2 - 1}} = b$$
$$b = \gamma\frac{(\varepsilon_r + 1)}{2\varepsilon_r}\;\frac{1}{3} \qquad (4)$$

where $\lambda = 2\pi/k$ is the free-space wavelength, $\lambda_{sw} = 2\pi/\beta_{sw}$ is the SW wavelength (with β_{sw} being the SW wavenumber), and $\gamma = v_0 p/h$. The above equation is obtained by approximating the cotangent function in the classical dispersion equation, see eq. (1) in [35], by its second order Taylor expansion for small arguments. One can observe in (4) that the ratio $\sigma = \lambda_{sw}/\lambda$ may be expressed as a function of either λ_{sw} or λ when the parameters ε_r and γ are fixed.

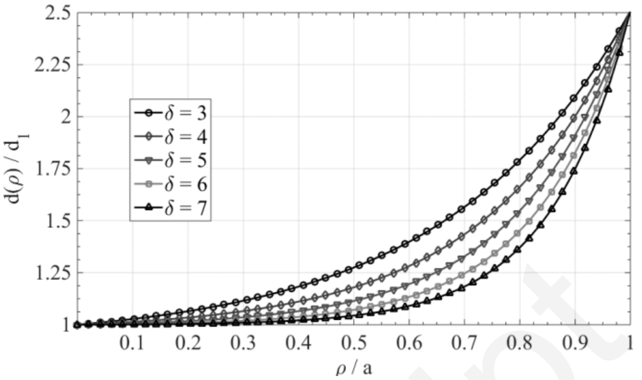

Fig. 3. Local period of the modulation as a function the radial distance ρ normalized to the antenna radius a, and for different values of the non-dimensional constant δ.

The geometrical parameter γ can be obtained from the full-wave analysis of a given metasurface element immersed in a periodic environment. The quantity σ is a "compression factor", always smaller than one, that serves to transform the dependence of the various parameters from SW wavelength to free-space wavelength. One can also interpret σ as the SW phase velocity normalized to the speed of light. Solving (4) for λ_{sw} as a function of σ, we obtain

$$\frac{\lambda_{sw}}{h} \doteq g_{sw}(\sigma) = \frac{\pi\left(\varepsilon_r\sigma^2 - 1\right)}{\varepsilon_r\sqrt{1-\sigma^2}}\left\{1 + \sqrt{1 + b4\varepsilon_r{}^2\,\frac{\left(1-\sigma^2\right)}{\left(\varepsilon_r\sigma^2 - 1\right)}}\right\} \qquad (5)$$

$$\frac{\lambda}{h} \doteq g(\sigma) = \frac{g_{sw}(\sigma)}{\sigma} \qquad (6)$$

Fig. 2(a) and Fig. 2(b) show the functions $g_{sw}{}^{-1}$ and g^{-1}, respectively, for several values of ε_r and for γ = 0.44 and γ = 4.

III. NON-UNIFORM MODULATION PERIODS AND UNIFORM AMPLITUDE OF THE -1 MODE

For the sake of clarity, we divide the presentation of the non-uniform modulation period between this section and Section IV. In this section, we will assume that the amplitude of the -1 Floquet mode remains uniform in the frequency range of interest. Although this condition is hard to obtain in practice over large bandwidths, it allows us to define a reference canonical solution that approximates the average gain and the gain bandwidth. This section does not discuss the type of amplitude modulation of the reactance needed to get this uniform amplitude. The amplitude modulation will be treated in Section IV.

A. *Exponential stretching of the modulation period*

The methodology to obtain a broadband response consists in compensating the variation of λ_{sw} with frequency. To this end, we impose an exponential variation of the period $d(\rho)$ of the transparent impedance versus the radial distance. This exponential function reads as:

$$d(\rho)=\left(\frac{d_1e^{\delta}-d_2}{\left(e^{\delta}-1\right)}\right)\quad\frac{\left(d_2-d_1\right)}{\left(e^{\delta}-1\right)}\quad{}^{\delta\rho/a}\qquad(7)$$

where δ is a non-dimensional constant that defines the speed of the exponential growth, while d_1 and d_2 are the values that the local period of the modulation takes at ρ=0 and ρ=a, i.e., $d_1=d(0),\ d_2=d(a)$.

One can find the corresponding phase function of the reactance by using (7) in (3) with $\Phi(0)=0$, and solving the integral in closed form as

$$\Phi(\rho)=2\pi\frac{\left(e^{\delta}-1\right)}{d_1e^{\delta}-d_2}\left(\rho-\frac{a}{\delta}\ln\frac{d(\rho)}{d_1}\right)\qquad(8)$$

The values of d_1 and d_2 must be selected to match the SW wavelength at the two different frequencies that determine the bandwidth. Fig. 3 presents $d(\rho)/d_1$ as a function of ρ/a for several values of the parameter δ. The inverse function of $d(\rho)$ can also be written in analytical form as

$$\rho\left(d\right)=\frac{a}{\delta}\ln\left[\frac{\left(d/d_1-1\right)\left(e^{\delta}-1\right)}{\left(d_2/d_1-1\right)}\quad 1\right]\qquad(9)$$

B. *Active region*

The strategy to enlarge the bandwidth is to impose a local matching between the SW wavelength and $d(\rho)$ on a given region of the circular aperture. Changing frequency implies a change of the wavelength-matched area. Therefore, the aperture behaves as an active region antenna in which the radiation mechanism is quite different from the well-known spiral antennas. Indeed, the SW (“0”-indexed Floquet mode) couples in the active region to the LW (“-1”-indexed Floquet mode), which radiates a broadside beam. Conversely, the radiation at broadside is quite low outside the annular active region due to the mismatch between the SW wavelength and the modulation period. Fig. 4 shows the phase relation between the reactance (red curve) and the SW field (blue curves) for different frequencies in the range of interest. The radius a of the antenna illustrated in Fig. 4 is a=5λ_{sw} at the minimum frequency and a=10λ_{sw} at the maximum frequency, while $d(\rho)$ has been calculated by setting δ=5 in (7). The radial distance ρ_0 represents the point of local phase matching, and it is located at the center of the active region.

The previous active region concept is formalized hereinafter in terms of the antenna’s aperture efficiency ε. The effective area of the antenna in absence of losses can be written as

$$A_{eff}=\pi a^2\varepsilon\qquad(10)$$

where the aperture efficiency ε[1] reads as

$$\varepsilon=\frac{4}{a^4\left(1-2d_2/a\right)}\left|\int_0^a e^{j\Psi(\rho)}\rho d\rho\right|^2\qquad(11)$$

The exponent $\psi(\rho)$ in (11) represents the phase of the -1 indexed Floquet mode, it may be approximated as

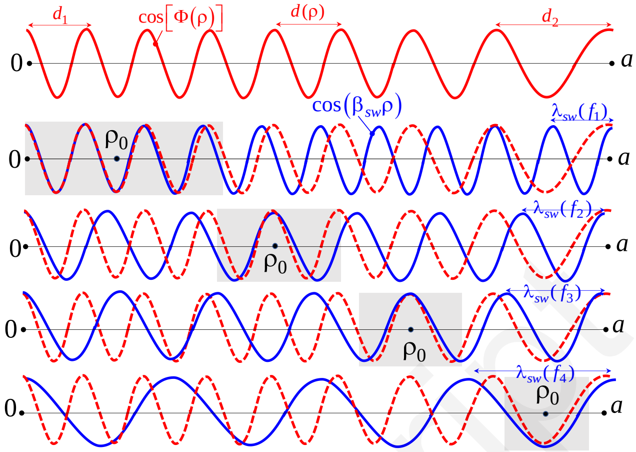

Fig. 4. Modulated reactance function $\cos(\Phi(\rho))$ (red lines) and SW E-field amplitude (blue lines) for several frequencies. The grey areas represent the radial extension of the active regions for each frequency, defined as the area where the phase of the SW matches the phase of the reactance with a predefined tolerance; ρ_0 denotes the central radial point of the active region.

$$\Psi(\rho)=\Phi(\rho)-\beta_{sw}\rho-\int_0^{\rho}\Delta\beta_{sw}\left(\rho'\right)d\rho'\qquad(12)$$

where $\Phi(\rho)$ is given by (8) and $\Delta\beta_{sw}$ is an incremental deviation of β_{sw} due to the modulation. One can estimate $\Delta\beta_{sw}$ as in [26]. Although $\Delta\beta_{sw}$ is normally much smaller than β_{sw}, the effect of its integration in (12) may be non-negligible in the proximity of the antenna rim. The stationary phase point condition $\Psi'(\rho_0)=0$, where the prime symbol indicates the derivative with respect to ρ, allows one to identify the center of the active region, ρ_0. The latter condition can also be written as

$$\Phi'(\rho_0)=\beta_{sw}+\Delta\beta_{sw}(\rho_0)\qquad(13)$$

By using (3) in (13), the stationary phase condition becomes

$$d\left(\rho_0\right)=\lambda_{sw}/(1+\Delta\beta_{sw}(\rho_0)/\beta_{sw})\approx\lambda_{sw}\qquad(14)$$

where $d(\rho)$ is given by (7). In other words, the stationary phase condition is equivalent to the matching condition of the local period with the SW wavelength at a certain frequency. According to (10), the length $L\approx A_{eff}/(2\pi a)=a\varepsilon/2$ is the effective radial extension of the active region, illustrated by the grey areas in Fig. 4.

C. *Uniform asymptotic evaluation*

The integral in (11) can be evaluated in analytical form by a uniform asymptotic stationary-phase approximation for large values of the parameter $\beta_{sw}a$. To this end, the phase is approximated around the stationary phase point ρ_0 as

$$\Psi(\rho)\approx-\xi_0\left(\rho-\rho_0\right)^2+\Psi_0\qquad(15)$$

where

$$\Psi_0=\Psi(\rho_0);\quad \xi_0=-\tfrac{1}{2}\Phi''(\rho_0)\qquad(16)$$

and the double prime symbol denotes the double derivative with respect to ρ. We can obtain the following explicit analytical expressions for ρ_0 and ξ_0 as a function of λ_{sw}

---

[1] Eq. (11) is obtained from the general form in (30) by assuming a constant S at the numerator and the function S given by (31) at the denominator.

$+\,|e$

$$\rho_0 \doteq \rho\left(\lambda_{sw}\right) = \frac{a}{\delta}\ln\left[\frac{\left(\lambda_{sw}/d_1-1\right)\left(e^{\delta}-1\right)}{\left(d_2/d_1-1\right)}+1\right] \tag{17}$$

$$\xi_0 \doteq \xi\left(\lambda_{sw}\right) = \pi\frac{\delta d_1}{a\lambda_{sw}{}^2}\left(\frac{\lambda_{sw}}{d_1}-1+\frac{\left(d_2/d_1-1\right)}{\left(e^{\delta}-1\right)}\right) \tag{18}$$

where (17) is found using (14) and (9), and $\xi(\lambda_{sw})$ is found by considering that $\xi(\lambda_{sw}) = -(2\pi/d(\rho))'/2$. It is interesting to note that both (17) and (18) can be also written as a function of the free-space wavelength by just using the compression factor in (6)

$$\rho_0 \doteq \rho\left(\lambda\sigma\left(\lambda\right)\right) \tag{19}$$

$$\xi_0 \doteq \xi\left(\lambda\sigma\left(\lambda\right)\right) \tag{20}$$

The uniform asymptotic evaluation of the integral in (11) yields

$$I \doteq \int_0^a e^{\mathrm{j}\Psi(\rho)}\rho\, d\rho \ \approx e^{\mathrm{j}\Psi_0}\frac{\rho_0\sqrt{\pi}}{\sqrt{j\xi_0}}F(\rho_0,\xi_0) \tag{21}$$

where

$$F(\rho_0,\xi_0) \approx 1-\frac{1}{2}\left[erfc\left(\sqrt{\mathrm{j}\xi_0}\,(a-\rho_0)\right)\right] \tag{22}$$

and $erfc\left(x\right)=\left(2/\sqrt{\pi}\right)\int_x^{\infty}e^{-t^2}dt$ is the complementary error function. The right hand side of (22) consists of two contributions: the first one is associated with the stationary phase point (located at center of the active region), whereas the second one is related to the endpoint in *a*. The latter contribution is interpreted as a diffracted field that leads to an unfocused spill-over of energy. At the higher frequency in the antenna bandwidth, the Fresnel-type transition function $F(\rho_0,\xi_0)$ goes to unity since the *erfc* function tends to vanish for $\rho_0 << a$. At the lower frequency in the bandwidth, ρ_0 approaches *a* and $F(\rho_0,\xi_0)$ gradually manages the transition of the active region out of the edge of the aperture. Using (21) in (11) leads to

$$\varepsilon \approx \frac{4}{a^4\left(1-2d_2/a\right)}\left|\frac{\rho_0\sqrt{\pi}}{\sqrt{\xi_0}}F\left(\rho_0,\xi\ \ \right)\right|^2 \tag{23}$$

The efficiency ε oscillates as a function of λ_{sw} around an average value. This average is obtained by substituting $\left|F(\rho_0,\xi_0)\right|=1$ in (23). From (17), the condition $\lambda_{sw}=d_2$ implies $\rho\left(\lambda_{sw}\right)=a$, which makes the argument of the *erfc* function in (22) vanishing; thus, leading to $\left|F(\rho_0,\xi_0)\right|=1/2$. This means that the efficiency is reduced of 6dB with respect to its average value when $\lambda_{sw}=d_2$. A better condition to identify the maximum wavelength $\lambda_{sw,\max}$ that gives the lower bound for the antenna bandwidth is $\left|1-erfc\left(\sqrt{\mathrm{j}t}\right)/2\right|=1/\sqrt{2}$, which implies $t=4/9$. Setting $t=4/9$ in the argument of the *erfc* function in (23) leads to

$$\rho\left(\lambda_{sw,\max}\right)=\frac{-4/9}{\sqrt{\xi\left(\lambda_{sw,\max}\right)}}\quad a \tag{24}$$

In the Appendix we show that it is possible to define an optimal value of δ for each d_2/d_1 ratio. The condition to choose the most favorable δ is to get $\rho_0/\sqrt{\xi_0}$ as linear as possible with wavelength, and is given by

$$\delta \doteq \delta_{opt} = \ln\left(\frac{d_2}{d_1}-0.984\right)+4.13 \tag{25}$$

Assuming $\delta=\delta_{opt}$, one may approximate the minimum wavelength, which gives the higher operating frequency, as

$$\lambda_{sw,\min} \approx 1.1d_1 \tag{26}$$

In turn, the maximum wavelength $\lambda_{sw,\max}$, related to the lower operating frequency, can be obtained by substituting (17) and (18) in (24).

D. Average gain

In this section, we identify the antenna gain with the directivity of the aperture. This identification implies an assumption of no-losses and an ideal feeder that provides a 100% efficiency in the transformation of the accepted power to SW power. The reader can find a complete study on the efficiency of the feeder and the effect of the losses in [23]. The average gain in the bandwidth is estimated as $G_{ave}=4\pi/\lambda^2A_{eff}=\left(2\pi a/\lambda\right)^2\varepsilon$, where ε is given by (23) with $\left|F\right|=1$. The broadside-direction average gain over the bandwidth takes the form

$$G_{ave} \approx \frac{a}{d_1}\frac{\left(4\pi\right)^2}{\left(1-2d_2/a\right)}\left[\frac{\sqrt{d_1\pi}\rho}{\lambda a\sqrt{a}\sqrt{\xi_0}}\right]^2 \tag{27}$$

In (27), the function between square brackets is quite constant with frequency for the value of $\delta=\delta_{opt}$ in (25). Eq. (44) in the Appendix shows that (27) can be approximated as

$$G_{ave} \approx \frac{a\left(4\pi\right)^2}{d_1\left[1-\frac{2d_2}{a}\right]}\frac{35\sigma^2_{\min}}{\left(\ln\left(\frac{d_2}{d_1}-0.984\right)\quad 4.13\right)^3} \tag{28}$$

where $\sigma_{\min}$ is the compression factor evaluated at $\lambda_{sw,\min}=1.1d_1$.

E. Bandwidth

To work in the range $\lambda_{\min}<\lambda<\lambda_{\max}$, see (24) and (26), the antenna will operate with λ_{sw} ranging from $1.1d_1$ to $\lambda_{sw,\max}$. Note that $\lambda_{sw,\max}$ does not coincide with d_2, since there must be an extra space to let the active region sliding out from the edge. Indeed, for $\lambda_{sw}=d_2$ the gain is reduced of 6dB with respect to the average value in (27). Defining the bandwidth parameter *B* as the ratio between the maximum and the minimum frequencies in the band of interest, one has

$$B=\frac{f_{\max}}{f_{\min}}=\frac{\lambda_{\max}}{\lambda_{\min}}=\frac{\lambda_{\mathrm{sw}\max}\sigma_{\min}}{\lambda_{\mathrm{sw}\min}\sigma_{\max}} \tag{29}$$

where $\sigma_{\max}$, $\sigma_{\min}$ are the compression factors associated with $\lambda_{sw,\max}$, $\lambda_{sw,\min}$. The wavelength $\lambda_{sw,\max}$ corresponds to the lower frequency of the operating bandwidth of the antenna.

IV. FREQUENCY DEPENDENT NON-UNIFORM MODULATION PERIODS AND NON-UNIFORM AMPLITUDE

The analysis presented in Section III is based on the assumption that the -1 Floquet mode presents a uniform amplitude that does not change with frequency. Such analysis is important, since it enables a fast preliminary design with simple convenient formulas. However, this uniform amplitude condition is quite difficult to obtain for large bandwidths. In this section, we present a more accurate model, accounting for both the amplitude and the phase variations of the -1 mode with frequency.

A. Amplitude and phase modulation at central frequency

In a more general case, where one cannot assume the amplitude of the aperture fields uniform and constant with frequency, we can obtain the efficiency as [23]

$$\varepsilon = \frac{2}{a^2}\frac{\left|\int_0^a \sqrt{S(\rho,\omega)}e^{j\Psi(\rho,\omega)}\rho d\rho\right|^2}{\int_0^a S(\rho,\omega)\rho d\rho} \tag{30}$$

where $S(\rho,\omega)$ is the *power density function* per unit surface [23] of the -1 mode, which depends on the radial distance ρ and on the angular frequency ω. In turn, the phase $\psi(\rho,\omega)$ maintains the definition in (12), although in (30) we have formally introduced the functional dependence with ω in the notation. Therefore, the efficiency in (30) depends on the frequency due to both the amplitude and the phase of the -1 Floquet mode.

In the first instance, we assume that it is possible to synthesize, at a center frequency $\omega=\omega_0$, a profile $S(\rho,\omega_0)$ which is mostly constant and goes to zero only the in proximity of the end-points 0 and a, namely [23]

$$\frac{S(\rho,\omega_0)}{S(0,\omega_0)} = \begin{cases} \sin^2(\pi\rho/d_1); & \rho \le 0.5d_1 \\ 1; & 0.5d_1 < \rho \le a-2d_2 \\ \sin^2\left[\frac{\pi}{4d_2}(a-\rho)\right]; & a-2d_2 < \rho \le a \end{cases} \tag{31}$$

Having the amplitude tapered to zero when $\rho=a$ serves to avoid the reduction of the antenna gain by spill-over at the rim of the MTS. The function $S(\rho,\omega_0)$ is plotted in Fig. 5(a). For convenience, the modulated reactance function $\cos(\Phi(\rho))$ is given in the same figure for $a=10d_1$ and $d_1/d_2=2.6$. We can also relate the power density function to the radial leakage attenuation parameter $\alpha(\rho)$ through [23]

$$\alpha(\rho,\omega_0) = \frac{\rho S(\rho,\omega_0)/2}{\frac{1}{2\pi}P_{sw} - \int_o^\rho S(\rho',\omega_0)\rho' d\rho'} \tag{32}$$

where P_{sw} is the power coupled by the source to the SW.

In order to obtain such a profile of $\alpha(\rho,\omega_0)$, one can prove [26] that the modulation index function $m(\rho)$ of the transparent reactance in (2) must present a profile that is approximately proportional to $\sqrt{\alpha(\rho)}$. A more accurate relation can be found solving the periodic problem that locally matches the periodicity $d(\rho)$ and the modulation index $m(\rho)$ (see inset in Fig. 1) and is characterized by the same transparent impedance. The solution of this problem provides the complex deviation of the "0"-mode wavenumber with respect to the wavenumber supported by the constant (non-modulated) average transparent reactance $\bar{X}_\rho$. The explicit formulation of this problem is given in [26], Sect. III and may be formally presented through the following functional dependences

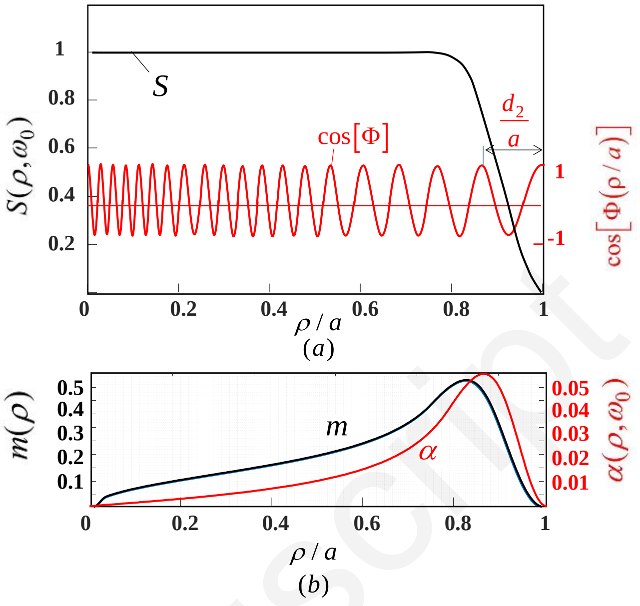

Fig. 5. (a) Power density function at the central frequency (black line, left vertical axis) and reactance modulation function (red line, right vertical axis). (b) Modulation index function (black line, left vertical axis) at the center frequency and value of $\alpha(\rho,\omega_0)/k$ (red line, right vertical axis).

$$\alpha = \mathrm{A}\left(m,\bar{X}_\rho,d,kh,\varepsilon_r\right) \tag{33}$$

$$\Delta\beta_{sw} = B\left(m,\bar{X}_\rho,d,kh,\varepsilon_r\right) \tag{34}$$

Eq. (33) has a formal inversion expression

$$m = \mathrm{A}^{-1}\left(\alpha,\bar{X}_\rho,d,kh,\varepsilon_r\right) \tag{35}$$

Nonetheless, we do not obtain (35) by functional inversion, but through a least-square approximation after the construction of a database from (33). This database can be built by using the dispersion equation in semi-analytical form (4), which requires the extraction of a single parameter from a full-wave analysis.

The profiles of $\alpha(\rho,\omega_0)$ and $m(\rho)$ presented in Fig. 5(b) allow one to obtain the power density function in Fig. 5(a). Both $\alpha(\rho,\omega_0)$ and $m(\rho)$ start from zero and increase up to their maximum value, which approximately occurs at the point in which the power density function starts to decrease.

B. Amplitude modulation as a function of frequency

The efficiency in (30) presents a frequency dependence due to both the power density and the phase in the integrals. The modulation index $m(\rho)$ can be considered constant when changing frequency. Conversely, α and $\Delta\beta_{sw}$ change on the basis of (33) and (34). Accounting for the variation with frequency of $\alpha(\rho,\omega)$, we can reconstruct a new $S(\rho,\omega)$ profile through the inverse formula of (32) (see [26], eq. (46)), i.e.

$$S(\rho,\omega) = 2\alpha(\rho,\omega)\frac{1}{\rho}\frac{P_{SW}}{2\pi}\exp\left(\;2\int_0^\rho \alpha(\rho',\omega)\;\;\rho'\right) \tag{36}$$

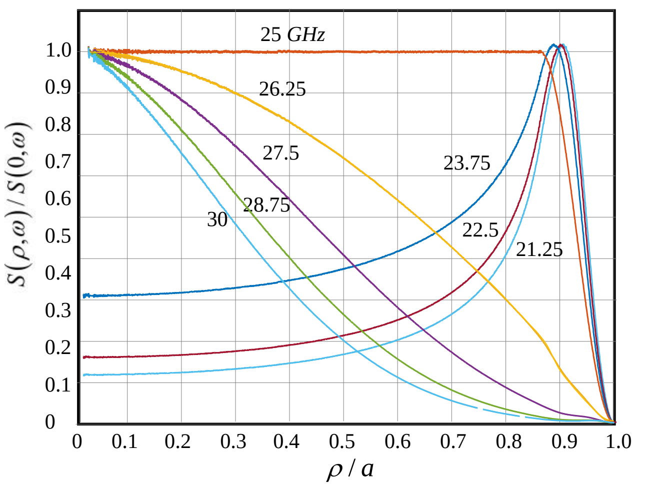

Fig. 6. Power density distribution for frequencies below and above 25GHz for a MTS antenna with m(ρ) designed at 25GHz, $\delta=\delta_{opt}$, and a=16.6cm.

The entire process actually depends on the angular frequency ω_0, at which we impose the profile of the power density given by (31). The value of ω_0 is a reference angular frequency between the maximum and minimum angular frequencies of the bandwidth. The steps followed to recover the profile of $S(\rho,\omega)$ as a function of frequency can be summarized as:

$$S(\rho,\omega_0)\xrightarrow{(32)}\alpha(\rho,\omega_0)\xrightarrow{(35)}m(\rho)\xrightarrow{(33)}\alpha(\rho,\omega)\xrightarrow{(6)}S(\rho,\omega) \quad (37)$$

Fig. 6 illustrates the outcome of the process described in (37), it shows the amplitude variation of $S(\rho)$ at different frequencies for an antenna with radius a=16.6cm. The substrate used in these calculations has a thickness h=0.635mm, and relative permittivity ε_r=6.15. The impedance at the central frequency of $\omega_0/(2\pi)$=25GHz exhibits a mean value $\bar{X}_\rho=-259.8\Omega$, while the modulation index $m(\rho)$ follows the profile in Fig. 5(b), and provides the distribution in (31) at ω_0. The phase of the impedance $\Phi(\rho)$ follows (8) with δ chosen as in (25). In Fig. 6, one can appreciate that the evolution of the power density with frequency follows the shift of the active region. For low frequencies $S(\rho)$ peaks at the edge of the aperture, it gradually becomes uniform at 25GHz, and for higher frequencies $S(\rho)$ is finally more concentrated close to the origin. In other words, the amplitude of the "-1"-mode follows the displacement of the active region, sliding inward/outward with the frequency, that is, most of the surface power density of the "-1"-mode is concentrated within the active region. This is a quite interesting result, and it may be justified by the local resonance effect between the surface impedance and the SW.

V. FULL-WAVE AND EXPERIMENTAL TESTING OF THE FORMULATION

In this Section, we validate the formulations presented in Sections III and IV. First, we use the full-wave method in [37] to calculate the gain versus frequency response and radiation patterns obtained with the homogenized transparent impedance in (2). Next, we implement these ideal impedances with elliptical elements to compare with the radiation patterns of an actual structure.

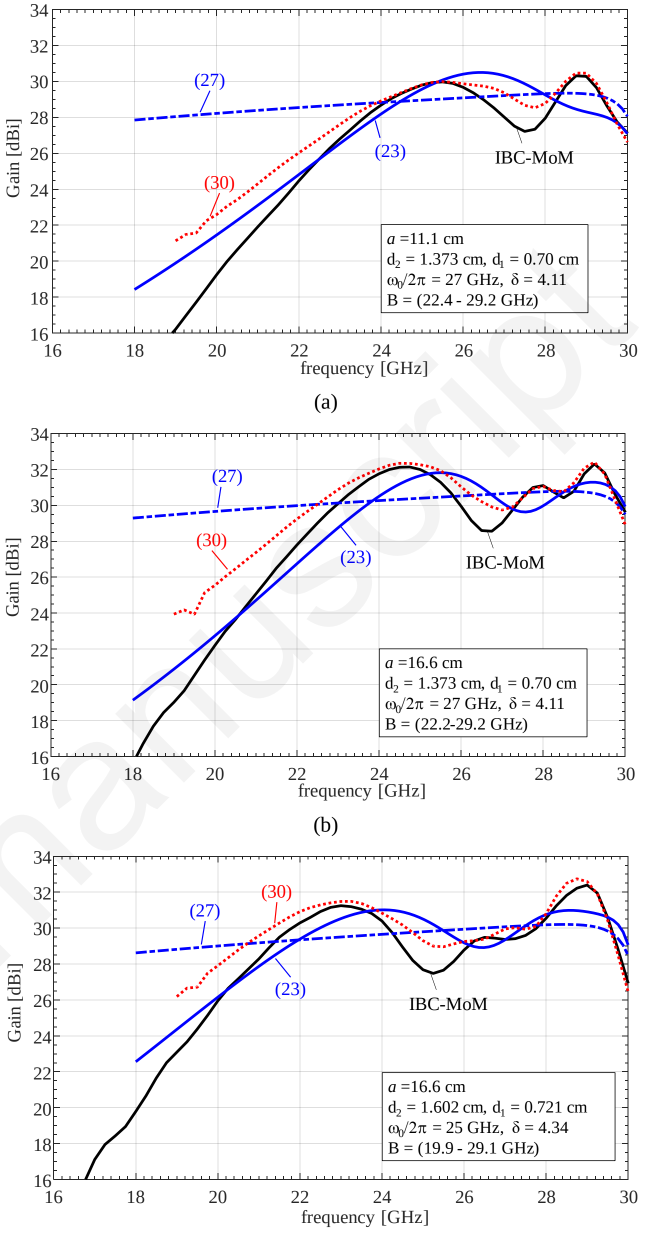

(c)

Fig. 7. Gain versus frequency responses for three different MTS antennas with $\delta=\delta_{opt}$ and: a) a=11.1 cm, d_1=7mm and d_2=13.7mm, (b) a=16.6 cm, d_1=7mm and d_2=13.7mm and (c) a=16.6 cm, d_1=7.21mm and d_2=16.02mm. Solid blue lines: closed-form transition-function formula for the efficiency in (23); dash-dotted blue lines: average gain formula in (27); short dashed red lines: eq. (30); black solid line: full wave MoM solution for the homogenized impedance. The insets show the bandwidth limits calculated with (24) and (26).

A. *Validation of the Formulations in Sections III and IV*

To test the formulation, we have carried out a full-wave analysis based on homogenized impedance. First, Fig. 7 presents the gain versus frequency response for three different configurations on the same substrate, with h=0.635mm and ε_r=6.15. All the analyzed cases provide a broadside pencil beam with right-handed circular polarization (RHCP). The radius of the antenna in Fig. 7(a) is a=11.1cm, while both Fig. 7(b) and Fig. 7(c) present results for antennas with a=16.6 cm.

Regarding the design of the ideal impedance planes, we have computed the phase function $\Phi(\rho)$ in (2) by substituting in (8): d_1=7mm and d_2=13.7mm for the examples in Fig. 7(a) and Fig. 7(b), and d_1=7.21 mm and d_2=16.02 mm for Fig. 7(c). In the three cases, we have used the value of the non-dimensional parameter δ computed by (25). The synthesis of the amplitude modulation function, $m(\rho)$, has been carried out at $\omega_0/(2\pi)$=27GHz for the antenna with a=11.1 cm in Fig. 7(a) and the antenna with a=16.6 cm in Fig. 7(b). Conversely, we have designed $m(\rho)$ at $\omega_0/(2\pi)$=25GHz for the antenna with a=16.6 cm in Fig. 7(c). The transparent impedances calculated at the nominal frequencies, i.e., 25GHz and 27GHz, have been used in (2) to compute modulated MTS reactance in the apertures.

Fig. 7(a), (b) and (c) show four different plots, which correspond to the gain versus frequency responses computed with the approximations in the previous sections. The solid blue lines were obtained using the closed-form transition-function formula for the efficiency ε in (23). The dash-dotted blue lines were computed using the simple average gain formula in (27). The short dashed red lines were calculated using (30) and the procedure summarized in (37). Finally, the solid black line shows the gain obtained with the MoM presented in [37] for circular apertures with homogenized modulated impedances. This technique uses an ideal feeding scheme, consisting of a vertical electric dipole (VED) placed at the antenna center, in the middle of the grounded slab. This VED acts as launcher for a cylindrical TM-SW. In this ideal case the gain (directivity) is obtained by

$$G=\frac{4\pi U_{\theta=0}}{\iint\limits_{4\pi} U(\theta,\phi)\sin\theta\, d\theta\, d\phi} \tag{38}$$

where $U(\theta,\varphi)$ is the power density per unit solid angle radiated in the far-field region by the equivalent electric currents obtained by the MoM solution. The radiated fields are computed by using the Green's function of the grounded slab.

Comparing the three cases, one can observe that the bandwidth increases for larger values of the ratio d_2/d_1. However, this bandwidth increment is accompanied by an oscillation versus frequency, which becomes more apparent for antennas with a larger radius. For instance, the amplitude of the oscillation around the average value in the gain versus frequency response in Fig. 7(a) is ±1.5 dB for an antenna with a=11.1cm, while for the 16.6 cm radius antenna in Fig. 7(b) this oscillation becomes ±2dB. Besides, it is important to note that (30), despite providing a moderately optimistic estimate of the lower frequency transition, works very well at the high frequency end of band of interest. On the other hand, the simple formulas in (27) and (24) and (26) allow one to make a fairly accurate estimation of the average gain and the bandwidth, respectively. Finally, using (28), one can predict G_{ave}=29.7 dB for the case with a=11.1 cm in Fig. 7(a), and G_{ave}=30 dB for the case with a=16.6 cm in Fig. 7(b).

To complete the analysis, Fig. 8 shows the co-polar (RHCP) and cross-polar (left-handed circular polarized, LHCP) components of the directivity patterns for the configurations

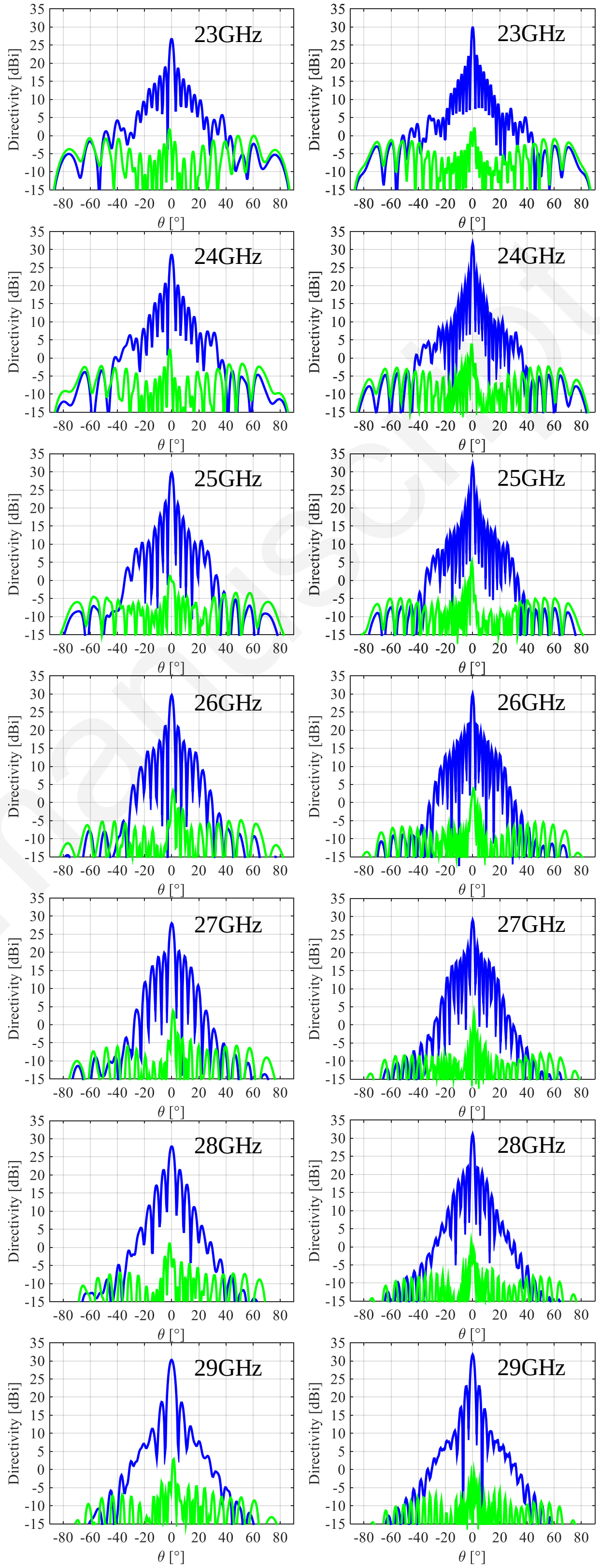

Fig. 8. Directivity patterns for the antennas in Fig. 7(a) and Fig. 7(b). Left and right columns correspond to the configuration in Fig. 7(a) (a=11.1cm, d_1=7mm, d_2=13.73mm) and Fig. 7(b) (a=16.6cm, d_1=7mm, d_2=13.73mm), respectively. Solid blue lines represent the co-polar (RHCP) components, while the solid green lines stand for the cross-polar (LHCP) ones.

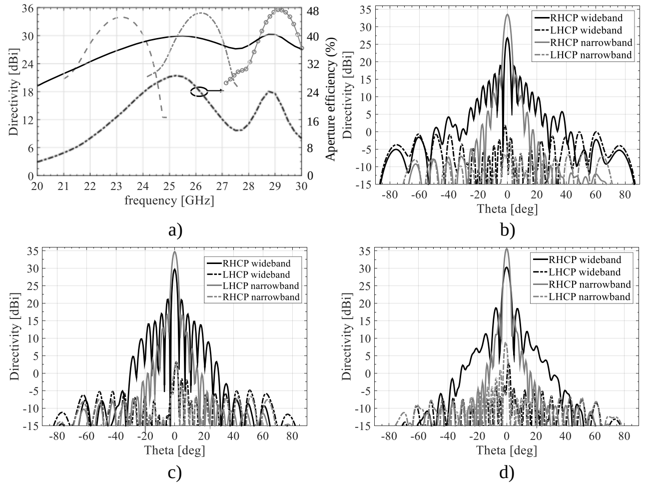

Fig. 9. (a) Directivity versus frequency responses for: the broadband design (solid black line) and the narrow-band designs at 23 GHz (dashed grey line), at 26 GHz (dash-dotted grey line) and at 29 GHz (grey line with markers). Comparison between the directivity patterns for the broadband and narrow-band designs at 23 GHz (b), 26 GHz (c) and 29 GHz (d).

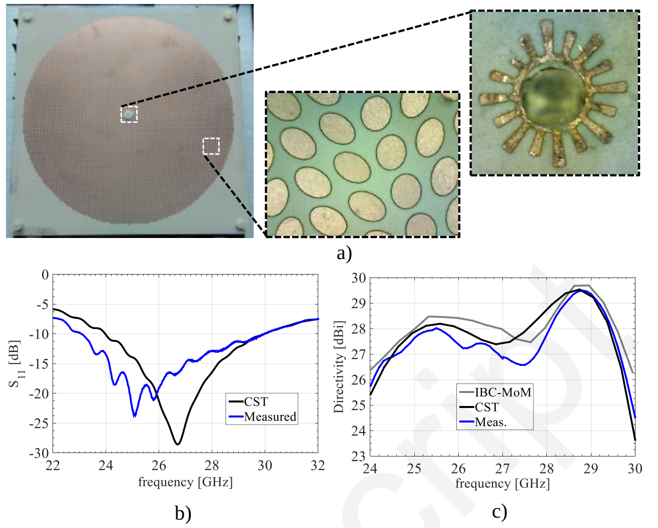

Fig. 10. (a) Fabricated prototype with zooms into the elliptical patches and the broadband feeder. (b) S_{11} in dB: measured (blue line) and computed with CST (black line). (c) Directivity versus frequency response: measured (blue line), calculated with CST (black line) and computed with the MoM in [37] (grey line).

described in Fig. 7(a) and (b). The patterns in the left column correspond to Fig. 7(a), while the patterns for the configuration in Fig. 7(b) appear in the right-hand side. In both cases, we have computed the in-band patterns with a 1GHz step. One can observe a good stability of the in-band pattern or, in other words, that the broadside pointing direction is preserved in the whole operating frequency range. Moreover, the cross-polarization discrimination is very good within all the frequency range of interest.

On the other hand, this class of MTS antenna trades aperture efficiency for bandwidth. To illustrate this tradeoff, Fig. 9(a) compares the directivity versus frequency response for the antenna in Fig. 7(a) (solid black line) with the responses obtained for three narrow-band designs with the same radius. These three antennas have been designed at 23, 26 and 29 GHz with a constant period, and for a maximum aperture efficiency. Fig. 9(a) also shows the aperture efficiency versus frequency for the broadband design (dash-dotted black line). The directivity and aperture efficiencies for the broadband and for the three narrowband designs are summarized in Table 1. In turn, Fig. 9(b), Fig. 9(c) and Fig. 9(d) present the comparison between the radiation patterns of the broadband design and those of the narrow-band antennas at 23, 26 and 29GHz, respectively.

Besides the lower directivity expected at broadside, one can observe that the broadband design presents higher side-lobes than the narrowband one. These side-lobes are due to two factors related to the active region architecture. On the one hand, the annular shape of the active region. Indeed, the Hankel transform of an annular region with uniform amplitude presents higher side-lobe levels than an equivalent circular region. On the other hand, the radiation of the non-active regions (even if weak) at a given frequency results in side-lobes.

Table 1. Summary with the directivity and aperture efficiencies calculated for the broadband and narrow-band designs at 23, 26 and 29GHz.

	Broadband		Narrow band	
Frequency (GHz)	Gain (dBi)	Aperture efficiency (%)	Gain (dBi)	Aperture efficiency (%)
23	26.8	16.7	33.8	83.8
26	29.7	25.4	34.9	83.2
29	30.3	23.5	35.6	78.9

B. *Experimental demonstration*

Finally, we have applied the proposed method to design a Ka-band modulated MTS antenna able to provide a RHCP broadside beam between 24GHz and 30GHz. We have synthesized the ideal impedance boundary condition with sub-wavelength elliptical patches [9] (see the inset in Fig. 10) printed on a Rogers RO3006™ substrate with h=0.635mm and ε_r=6.15, also used in the previous sections. Fig. 10(a) shows the fabricated prototype, including a zoom into the elliptical patches (center) and into the feeder (right). In turn, Fig. 10(b) presents the magnitude of the input reflection coefficient calculated with CST Microwave Studio [38] (black line) and measured (blue line). Both curves show a reflection coefficient lower than -10 dB in the operating frequency range. The curves match well, apart from a small frequency shift due to the assembly of the broadband feeder. In Fig. 10(c), one can see the comparison between the directivity versus frequency response calculated with the MoM tool in [37] (grey line), with CST (black line) and measured (blue line). The latter curves are also in good agreement, except for the slightly higher directivity values predicted by the MoM code and CST.

Fig. 11 presents the directivity patterns in one of the principal planes computed within the frequency range of interest with a step of 1GHz. Each subfigure shows a comparison between the results obtained with the MoM tool in [37] (grey lines), also used in Section V-A to validate the gain

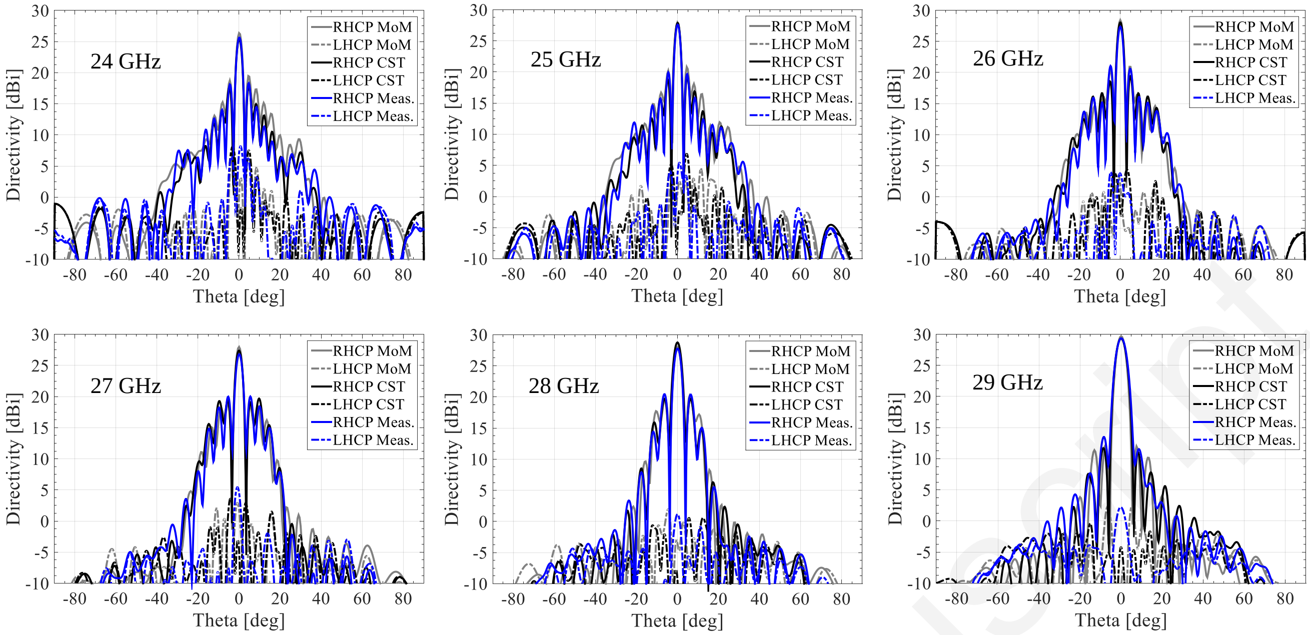

Fig. 11 Gain patterns for the broadband MTS antenna prototype presented in subsection B at several frequencies: from 24 to 29 GHz, with 1GHz step. The black solid lines and the black dashed lines represent the RHCP and the LHCP components calculated with CST. In turn, the grey solid lines and the grey dotted lines represent the RHCP and the LHCP components calculated with the homogenized boundary condition MoM technique in [37]. Finally, blue solid lines and blue dashed lines represent the broadband antenna measured gain patterns.

formulas, CST Microwave Studio [38] (black lines) and with the measurements (blue lines). The antenna has a radius a=11.1cm, like the case presented in Fig. 7(a) and in the left column of Fig. 8. The directivity patterns obtained with the numerical methods are in a very good agreement with the measurements, which constitutes an additional cross-check for the results in the previous section.

VI. CONCLUSION

This paper presents a simple method to enlarge the bandwidth of modulated metasurface (MTS) antennas by varying the period of the modulation along the radial distance in circular apertures. We have also introduced two simple models to enable an efficient analysis and design of this class of antennas. In the first model, one carries out an asymptotic evaluation of the integral that approximates the aperture efficiency to obtain simple design formulas. The second model provides a better accuracy at the expense of a moderately higher complexity in the analysis. This analysis implies the solution of the canonical problems that locally match the modulation, as done in [26] for the flat optics analysis. Both models have been validated using the MoM tool in [37] to analyze the continuous aperture reactance that provides wideband operation. In addition, we have presented full-wave simulations and measurements for a design example consisting of an 11.1cm radius aperture synthesized with sub-wavelength patches printed on a grounded substrate, and excited by a realistic feed. The proposed method features a very good pattern stability, and a gain versus frequency that can easily reach an average gain of 30 ± 1.5 dB over a 30% bandwidth (see Fig. 7(b)). Such performance is very difficult to reach by flat antennas with comparable technology and costs. This achievement extends significantly the range of applications for MTS antennas. Nonetheless, as expected, the broader bandwidth is obtained at the expense of reducing the aperture efficiency and higher side lobe levels. For instance, the example in Fig. 7(b) yields an in-band average efficiency around 25%.

Although this work has focused on broadside beams, one could also extend the methodology to tilted beams. An important additional point consists in controlling the side lobe over the bandwidth. Both aspects are subjects under investigation for future improvements.

ACKNOWLEDGEMENTS

The authors would like to thank the M^{2}ARS platform of the Institut d'Électronique et de Télécommunications de Rennes (IETR). In particular, they want to express their gratitude to Dr. Laurent Le Coq (Université de Rennes 1) for carrying out the measurements shown in Section V-B at IETR's CAMILL facility. The authors are also thankful to Christophe Guitton and Frédéric Boutet (Université de Rennes 1) for assembling the prototype. Finally, the authors would like to thank Mr. Adrian Lamoral-Coines for his help in the design of the broadband feed.

APPENDIX

In (23), the efficiency depends on $F(\rho_0,\xi_0)$, both ρ_0 and ξ_0 are function of λ_{sw}. One can also obtain these functions in terms of λ through (19) and (20). In the region $\lambda_{sw,\min} < \lambda_{sw} < \lambda_{sw,\max}$ (delimited by (24) and (26)), and by substituting the expressions for ρ_0 and ξ_0 in (17) and (18), respectively, one can write

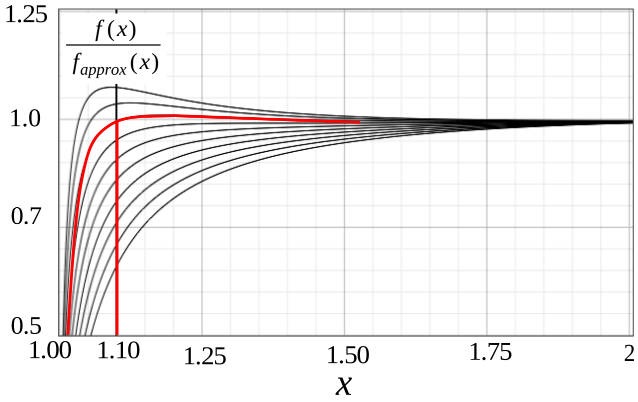

Fig. 12. Function f(x) that represents the dominant stationary phase contribution, normalized with respect to its asymptotic approximation $f_{approx}(x)$ as a function of x. The ratio d_2/d_1=2.5 and the solid black lines have been obtained for different values of τ. The solid red line highlights f(x) for $\delta=\delta_{opt}$.

$$\approx \frac{4d_1}{a\left(1-2d_2/a\right)}\left| \quad (\lambda_{sw}/d_1)\right|^2 \tag{39}$$

where

$$f(x) \doteq \frac{x\ln\left[\frac{1}{\tau}\left(x-1\right)+1\right]}{\delta^{3/2}\sqrt{\left(x-1+\tau\right)}} \tag{40}$$

and $\tau=\left(d_2/d_1-1\right)\left(e^{\delta}-1\right)^{-1}$. For large values of x, (40) exhibits a linear behavior that can be approximated as

$$f(x) \approx f_{approx}(x) \doteq \delta^{-3/2}\left[(x-2)q+b\right] \tag{41}$$

where $q=3\ln\left[2/\tau\right]/\sqrt{2}-2\ln\left[1/\right]\tau$ and $b=2\ln\left[1/\tau\right]$. Fig. 12 shows the function $f(x)/f_{approx}(x)$ for d_2/d_1=2.5 and δ ranging from 3 to 5. One can appreciate that for each value of the stretching ratio d_2/d_1, there exists a value of δ for which the linear approximation in (41) is valid in a larger range. This value provides the larger bandwidth extension towards lower frequencies. The value of δ which provides the largest linear range is found for any value of d_2/d_1 by fixing τ=0.016. Such choice provides an extension of the region in which $f(x)$ in (40) can be approximated by the linear function in (41) to x=1.1, and a sharp drop-off to zero at x=1. Therefore, the condition τ=0.016 leads to an optimal value of δ for any d_2/d_1 ratio as

$$\delta \doteq \delta_{opt} = \ln\left(\frac{d_2}{d_1}-0.984\right)+4.13 \tag{42}$$

The so-obtained δ_{opt} is the optimal choice for maximizing the product bandwidth–gain.

Using δ_{opt} in (41) $f_{approx}(x)$ becomes

$$f_{approx}(x) = \delta_{opt}{}^{-3/2}\left[1.97x+4.33\right] \tag{43}$$

Thus, the average gain in (27) can be rewritten as

$$G_{ave} \approx \frac{a}{d_1}\frac{(4\pi)^2}{(1-2d_2/a)}\left|f(\lambda_{sw}/d_1)\right|^2 \tag{44}$$

In the frequency range delimited by $\lambda_{sw,\min}$ and $\lambda_{sw,\max}$, G_{ave} can be well approximated as

$$f_{sw}(x) \approx \frac{\sigma(x)}{x}\delta_{opt}{}^{-3/2}\left[1.97x \quad 4.33\right] \tag{45}$$

where $\sigma(x)$ is the compression ratio function in (6). The function given by (44) is flat in the frequency range from $\lambda_{sw,\min}$ to $\lambda_{sw,\max}$. Therefore, the in-band value of (44) can be calculated at an arbitrary point within the defined bandwidth, for instance at the lower corner point $\lambda_{sw}=\lambda_{sw\min}=1.1d_1$. Substituting $f(1.1)\approx 6.5\delta_{opt}{}^{-3/2}$ in (44), one arrives to the expression (28).

REFERENCES

[1] C. Holloway, E. F. Kuester, J. Gordon, J. O’Hara, J. Booth, and D. Smith, “An overview of the theory and applications of metasurfaces: The two-dimensional equivalents of metamaterials,” *IEEE Antennas Propag. Mag.*, vol. 54, no. 2, pp. 10–35, Apr. 2012.

[2] M. Selvanayagam and G. V. Eleftheriades, “Discontinuous electromagnetic fields using orthogonal electric and magnetic currents for wavefront manipulation,” *Opt. Express*, vol. 21, pp. 14409-14429, 2013.

[3] N. Yu et al., “Flat optics: Controlling wavefronts with optical antenna metasurfaces,” *IEEE J. Sel. Topics Quantum Electron.*, vol. 19, no. 3, 4700423 pp., May 2013.

[4] S. B. Glybovski, S. A. Tretyakov, P. A. Belov, Y. S. Kivshar, and C. R. Simovski, “Metasurfaces: From microwaves to visible,” *Phys. Rep.*, vol. 634, pp. 1-72, 2016.

[5] A. Li, S. Singh, and D. Sievenpiper, “Metasurfaces and their applications,” *Nanophoton.*, vol. 7, no. 6, pp. 989-1011, 2018.

[6] S. Maci, G. Minatti, M. Casaletti, and M. Bosiljevac, “Metasurfing: Addressing waves on impenetrable metasurfaces,” *IEEE Antennas Wireless Propag. Lett.*, vol. 10, pp. 1499–1502, 2011.

[7] A. M. Patel and A. Grbic, “Effective surface impedance of a printed circuit tensor impedance surface (PCTIS),” *IEEE Trans. Microw. Theory Tech.*, vol. 61, no. 4, pp. 1403–1413, Apr. 2013.

[8] A. M. Patel and A. Grbic, “The effects of spatial dispersion on power flow along a printed-circuit tensor impedance surface,” *IEEE Trans. Antennas Propag.*, vol. 62, no. 3, pp. 1464-1469, Mar. 2014.

[9] M. Mencagli, Jr., E. Martini, and S. Maci, “Surface wave dispersion for anisotropic metasurfaces constituted by elliptical patches,” *IEEE Trans. Antennas Propag.*, vol. 63, no. 7, pp. 2992–3003, Jul. 2015.

[10] E. Martini, M. Mencagli, D. González-Ovejero and S. Maci, “Flat optics for surface waves,” *IEEE Trans. Antennas Propag.*, vol. 64, no. 1, pp. 155-166, Jan. 2016.

[11] Y. B. Li, R. Y. Wu, W. Wu, C. B. Shi, Q. Cheng, and T. J. Cui, “Dual-physics manipulation of electromagnetic waves by system-level design of metasurfaces to reach extreme control of radiation beams,” *Adv. Mater. Technol.*, vol. 2, no. 1, pp. 1600196, 2017.

[12] B. H. Fong, J. S. Colburn, J. J. Ottusch, J. L. Visher, and D. F. Sievenpiper, “Scalar and tensor holographic artificial impedance surfaces,” *IEEE Trans. Antennas Propag.*, vol. 58, no. 10, 435 pp. 3212–3221, Oct. 2010.

[13] A. M. Patel and A. Grbic, “A printed leaky-wave antenna based on a sinusoidally-modulated reactance surface,” *IEEE Trans. Antennas Propag.*, vol. 59, no. 6, pp. 2087–2096, Jun. 2011.

[14] G. Minatti, F. Caminita, M. Casaletti, and S. Maci, “Spiral leaky-wave antennas based on modulated surface impedance,” *IEEE Trans. Antennas Propag.*, vol. 59, no. 12, pp. 4436–4444, Dec. 2011.

[15] G. Minatti, S. Maci, P. De Vita, A. Freni, and M. Sabbadini, “A circularly-polarized isoflux antenna based on anisotropic metasurface,” *IEEE Trans. Antennas Propag.*, vol. 60, no. 11, pp. 4998–5009, Nov. 2012.

[16] G. Minatti et al., “Modulated metasurface antennas for space: Synthesis, analysis and realizations,” *IEEE Trans. Antennas Propag.*, vol. 63, no. 4, pp. 1288–1300, Apr. 2015.

[17] S. Pandi, C. A. Balanis, and C. R. Birtcher, “Design of scalar impedance holographic metasurfaces for antenna beam formation with desired polarization,” *IEEE Trans. Antennas Propag.*, vol. 63, no. 7, pp. 3016–3024, Jul. 2015.

[18] M. Faenzi et al., “Realization and measurement of broadside beam modulated metasurface antennas,” *IEEE Antennas Wireless Propag. Lett.*, vol. 15, pp. 610–613, 2016.

[19] G. Minatti et al., “Metasurface antennas,” in *Aperture Antennas for Millimeter and Sub-Millimeter Wave Applications*, A. Boriskin and R. Sauleau, Eds. Cham, Switzerland: Springer, 2018, ch. 9, pp. 289–333.

[20] E. Abdo-Sánchez, M. Chen, A. Epstein and G. V. Eleftheriades, “A leaky-wave antenna with controlled radiation using a bianisotropic Huygens’ metasurface,” *IEEE Trans. Antennas Propag.*, vol. 67, no. 1, pp. 108-120, Jan. 2019.

[21] D. González-Ovejero, T. J. Reck, C. D. Jung-Kubiak, M. Alonso-DelPino, and G. Chattopadhyay, “A class of silicon micromachined metasurface for the design of high-gain terahertz antennas,” in *Proc. IEEE Int. Symp. Antennas Propag.*, Fajardo, Puerto Rico, Jun./Jul. 2016, pp. 1191–1192.

[22] D. González-Ovejero, N.Chahat, R. Sauleau, G. Chattopadhyay, S. Maci and M. Ettorre, “Additive Manufactured Metal-Only Modulated Metasurface Antennas,” *IEEE Trans. Antennas Propag.*, vol. 66, no. 11, pp. 6106-6114, Nov. 2018.

[23] G. Minatti, E. Martini and S. Maci, “Efficiency of metasurface antennas,” *IEEE Trans. Antennas Propag.*, vol. 65, no. 4, pp. 1532-1541, April 2017.

[24] A. T. Pereda et al., “Dual circularly polarized broadside beam metasurface antenna,” *IEEE Trans. Antennas Propag.*, vol. 64, no. 7, pp. 2944–2953, Jul. 2016.

[25] M. Li, S. Xiao and D. F. Sievenpiper, “Polarization-insensitive holographic surfaces with broadside radiation,” *IEEE Trans. Antennas Propag.*, vol. 64, no. 12, pp. 5272-5280, Dec. 2016.

[26] G. Minatti, F. Caminita, E. Martini, and S. Maci, “Flat optics for leaky waves on modulated metasurfaces: Adiabatic Floquet-wave analysis,” *IEEE Trans. Antennas Propag.*, vol. 64, no. 9, pp. 3896–3906, Sep. 2016.

[27] G. Minatti, F. Caminita, E. Martini, M. Sabbadini, and S. Maci, “Synthesis of modulated-metasurface antennas with amplitude, phase, and polarization control,” *IEEE Trans. Antennas Propag.*, vol. 64, no. 9, pp. 3907–3919, Sep. 2016

[28] D. González-Ovejero, G. Minatti, G. Chattopadhyay, and S. Maci, “Multibeam by metasurface antennas,” *IEEE Trans. Antennas Propag.*, vol. 65, no. 6, pp. 2923–2930, Jun. 2017.

[29] Y. B. Li, X. Wan, B. G. Cai, Q. Cheng, and T. J. Cui, “Frequency-controls of electromagnetic multi-beam scanning by metasurfaces,” *Sci. Rep.*, vol. 4, Nov. 2014, Art. no. 6921.

[30] X. Wan, et al. “Manipulations of dual beams with dual polarizations by full-tensor metasurfaces,” *Adv. Opt. Mater.*, vol. 4, no. 10, pp. 1567-1572, Jun. 2016.

[31] M. Faenzi, D. González-Ovejero, F. Caminita, and S. Maci, “Dual-band self-diplexed modulated metasurface antennas,” in *Proc. 12nd Eur. Conf. Antennas Propag.*, London, 2018

[32] Y. Li, A. Li, T. Cui and D. F. Sievenpiper, “Multiwavelength Multiplexing Hologram Designed Using Impedance Metasurfaces,” *IEEE Trans. Antennas Propag.*, vol. 66, no. 11, pp. 6408-6413, Nov. 2018.

[33] S. Pandi, C. A. Balanis and C. R. Birtcher, “Analysis of Wideband Multilayered Sinusoidally Modulated Metasurface,” *IEEE Antennas Wireless Propag. Lett.*, vol. 15, pp. 1491-1494, 2016.

[34] G. Minatti, M. Faenzi, M. Sabbadini and S. Maci, “Bandwidth of gain in metasurface antennas,” *IEEE Trans. Antennas Propag.*, vol. 65, no. 6, pp. 2836-2842, Jun. 2017.

[35] M. Mencagli, Jr., E. Martini, and S. Maci, “Transition function for closed-form representation of metasurface reactance,” *IEEE Trans. Antennas Propag.*, vol. 64, no. 1, pp. 136–145, Jan. 2016.

[36] M. Mencagli, C. D. Giovampaola, and S. Maci, “A closed-form representation of isofrequency dispersion curve and group velocity for surface waves supported by anisotropic and spatially dispersive metasurfaces,” *IEEE Trans. Antennas Propag.*, vol. 64, no. 6, pp. 2319–2327, Jun. 2016.

[37] D. González-Ovejero and S. Maci, “Gaussian ring basis functions for the analysis of modulated metasurface antennas,” *IEEE Trans. Antennas Propag.*, vol. 63, no. 9, pp. 3982–3993, Sep. 2015.

[38] CST of America, “CST Microwave Studio,” Anaheim, CA, 2016.

Marco Faenzi was born in Siena, Italy. He received the M.Sc. degree in telecommunications engineering (with a score of 110/110) from the Dept. of Information Engineering and Mathematics of the University of Siena, Siena, Italy, in 2011. In the same year, he won a Ph.D. position at the Dept. of Information Engineering and Mathematics of the University of Siena to develop high-gain modulated metasurface antennas for space. After receiving his Ph.D. degree in 2015, he obtained a Post-Doctoral fellowship co-financed by the European Space Agency and the University of Siena in the framework of a Networking/Partnering Initiative. He currently works as a Post-Doctoral researcher at the Institut d’Électronique et de Télécommunications de Rennes, France. He has worked on optimizing the aperture efficiency of metasurface holographic antennas and, during his Post-Doctoral appointments, towards the characterization, optimization and synthesis of multi-band and broadband modulated metasurface apertures. He has also applied metasurface technology to the implementation of multibeam and high- efficiency monopulse antennas with linear and circular polarization.

Dr. Faenzi was a recipient of the Sergei A. Schelkunoff Transactions Prize Paper Award from the IEEE Antennas and Propagation Society in 2016.

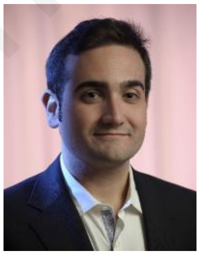

David González-Ovejero (S’01–M’13–SM’17) was born in Gandía, Spain, in 1982. He received the M.S. degree in telecommunication engineering from the Universidad Politécnica de Valencia, Valencia, Spain, in 2005, and the Ph.D. degree in electrical engineering from the Université catholique de Louvain, Louvain-la-Neuve, Belgium, in 2012.

From 2006 to 2007, he was a Research Assistant with the Universidad Politécnica de Valencia. From 2007 to 2012, he was a Research Assistant with the Université catholique de Louvain. From 2012 to 2014, he was a Research Associate with the University of Siena, Siena, Italy. In 2014, he joined the Jet Propulsion Laboratory, California Institute of Technology, Pasadena, CA, USA, where he was a Marie Curie Post-Doctoral Fellow. Since 2016, he has been a tenured researcher with the French National Center for Scientific Research, Institut d’Electronique et de Télécommunications de Rennes, Rennes, France.

Dr. González-Ovejero was a recipient of a Marie Curie International Outgoing Fellowship from the European Commission 2013, the Sergei A. Schelkunoff Transactions Prize Paper Award from the IEEE Antennas and Propagation Society in 2016, and the Best Paper Award in Antenna Design and Applications at the 11th European Conference on Antennas and Propagation in 2017.

Stefano Maci (M’92–SM’99–F’04) received the Laurea degree (cum laude) in electronics engineering from the University of Florence, Florence, Italy, in 1987.

Since 1997, he has been a Professor with the University of Siena, Siena, Italy. His current research interests include high-frequency and beam representation methods, computational electromagnetics, large phased arrays, planar antennas, reflector antennas and feeds, metamaterials, and metasurfaces.

Prof. Maci was a recipient of the European Association on Antennas and Propagation (EurAAP) Award in 2014, the Sergei A. Schelkunoff Transactions Prize Paper Award, and the Chen-To Tai Distinguished Educator Award from the IEEE Antennas and Propagation Society (IEEE AP-S) in 2016. Since 2000, he has been a member of the Technical Advisory Board of 11 international conferences and the Review Board of 6 International Journals. He has organized 25 special sessions in international conferences and held 10 short courses in the IEEE AP-S Symposia about metamaterials, antennas, and computational electromagnetics. In 2004, he was the Founder of the European School of Antennas, a postgraduate school that presently comprises 30 courses on antennas, propagation, electromagnetic theory, and computational electromagnetics, with 150 teachers from 15 countries. From 2004 to 2007, he was a WP Leader of the Antenna Center of Excellence (ACE, FP6-EU) and the International Coordinator of a 24-institution consortium of a Marie Curie Action (FP6) from 2007 to 2010. Since 2010, he has been a Principal Investigator of six cooperative projects financed by the European Space Agency. He has been the Director of the University of Siena’s Ph.D. program in information engineering and mathematics from 2008 to 2015, and a member of the National Italian Committee for Qualification to Professor from 2013 to 2015. He is the Director of the consortium FORESEEN, which currently consists of 48 European institutions, and a Principal Investigator of the Future Emerging Technology project Nanoarchitectronics of the 8th EU Framework program. He was a Co-Founder of two spin-off companies. He is a Distinguished Lecturer of the IEEE AP-S and of EuRAAP. He was a former member of the IEEE AP-S AdCom, EurAAP Board of Directors, and Antennas and Propagation Executive Board of the Institution of Engineering and Technology, U.K. He was an Associate Editor of the IEEE TRANSACTIONS ON ANTENNAS AND PROPAGATION and the Chair of the Award Committee of IEEE AP-S. He has co-authored over 150 papers published in international journals, among which 100 are in IEEE journals, 10 book chapters, and about 400 papers in proceedings of international conferences. These papers have received around 6700 citations.